


 Cite this: *RSC Adv.*, 2022, 12, 5094

Highly active postspinel-structured catalysts for oxygen evolution reaction†

 Yuichi Okazaki,^a Seiji Oda,^a Akihiko Takamatsu,^b Shogo Kawaguchi,^c Hirofumi Tsukasaki,^a Shigeo Mori,^a Shunsuke Yagi,^d Hidekazu Ikeno^{*ae} and Ikuya Yamada^{id} ^{*a}

The rational design principle of highly active catalysts for the oxygen evolution reaction (OER) is desired because of its versatility for energy-conversion applications. Postspinel-structured oxides, CaB_2O_4 ($B = \text{Cr}^{3+}$, Mn^{3+} , and Fe^{3+}), have exhibited higher OER activities than nominally isoelectronic conventional counterparts of perovskite oxides LaBO_3 and spinel oxides ZnB_2O_4 . Electrochemical impedance spectroscopy reveals that the higher OER activities for CaB_2O_4 series are attributed to the lower charge-transfer resistances. A density-functional-theory calculation proposes a novel mechanism associated with lattice oxygen pairing with adsorbed oxygen, demonstrating the lowest theoretical OER overpotential than other mechanisms examined in this study. This finding proposes a structure-driven design of electrocatalysts associated with a novel OER mechanism.

 Received 21st January 2022
 Accepted 1st February 2022

DOI: 10.1039/d2ra00448h

rsc.li/rsc-advances

Introduction

The oxygen evolution reaction (OER: $4\text{OH}^- \rightarrow \text{O}_2 + 2\text{H}_2\text{O} + 4\text{e}^-$ in alkaline conditions) plays an essential role in energy-conversion applications such as water electrolysis and rechargeable metal–air batteries.^{1–3} Since this reaction intrinsically involves large overpotentials causing colossal energy loss, precious-metal oxides (*e.g.*, RuO_2 and IrO_2) are presently utilized as typical OER catalysts.^{4–6} Despite their high performance, large-scale applications are restricted because of their scarcity and high cost. Accordingly, much effort has been directed toward the development of highly active transition metal oxide catalysts consisting of earth-abundant and low-cost elements.^{7,8} Most of the transition metal oxide catalysts, such as spinel and perovskite, comprise tetrahedral and octahedral metal–oxygen units.^{1,9–11} The perovskite-structured oxides, one

of the most well-studied experimentally and theoretically catalyst systems,^{1,12} consist of vertex-sharing octahedra, in which a single-site adsorption/reaction mechanism is widely accepted as adsorbates evolution reaction (AEM).^{12,13} The reactants are adsorbed on coordinatively unsaturated sites (CUS) formed by the extraction of oxygen at an octahedral vertex. Since the neighboring transition metal sites in vertex-sharing octahedra are far from each other, the bridging adsorption of adsorbates on two active sites is disturbed.

Several structures in transition metal oxides possess particular geometric conditions such as smaller transition-metal interatomic distances than that of vertex-sharing octahedra in perovskite, inducing interactions between adsorbates and multiple sites on the catalyst surface. Accordingly, dual-site adsorption/reaction mechanisms that the reactant bound to the CUS is also connected to another atom in the surrounding polyhedra are manifested by experiments and theoretical calculations.^{5,14–17} For example, the dual-site reaction mechanism bridging *B*-site octahedral CUS metal and *A'*-site pseudo-square coordinated transition metal has been suggested in the *A*-site-ordered quadruple perovskite ($\text{AA}'_3\text{B}_4\text{O}_{12}$).^{15,16} The dual-site reaction mechanism has been experimentally and theoretically examined in the rutile-structured RuO_2 .^{5,18} RuO_2 is composed of one-dimensional edge-shared RuO_6 octahedral chains gathered by sharing vertices. The reaction mechanism reported in the $\text{RuO}_2(110)$ surface involves a reaction step where an oxygen atom adsorbed on the Ru CUS combines with the oxygen atom (O_{BRI}) bridging two Ru atoms in the octahedral chain neighboring to CUS.⁵ Recently, Sugawara *et al.* reported that CaFe_2O_4 exhibits higher OER activity than other Fe oxides,¹⁷ suggesting a novel reaction mechanism in which three Fe atoms

^aDepartment of Materials Science, Graduate School of Engineering, Osaka Prefecture University, 1-1 Gakuen-cho, Naka-ku, Sakai, Osaka 599-8531, Japan. E-mail: yamada@mtr.osakafu-u.ac.jp; ikeno@mtr.osakafu-u.ac.jp

^bDepartment of Molecular Engineering, Graduate School of Engineering, Kyoto University, Kyoto Daigaku Katsura, Saikyo-ku, Kyoto 615-8510, Japan

^cJapan Synchrotron Radiation Research Institute (JASRI), 1-1-1 Kouto, Sayo-cho, Sayo-gun, Hyogo 679-5198, Japan

^dInstitute of Industrial Science, The University of Tokyo, 4-6-1 Komaba, Meguro-ku, Tokyo 153-8505, Japan

^ePrecursory Research for Embryonic Science and Technology (PRESTO), Japan Science and Technology Agency (JST), 4-1-8 Honcho Kawaguchi, Saitama 332-0012, Japan

† Electronic supplementary information (ESI) available: Structural parameters and refined profiles in Rietveld refinements are displayed for all the samples. The SEM and HRTEM images show the morphology of all samples. The calculated values and conditions of DFT calculations. See DOI: 10.1039/d2ra00448h



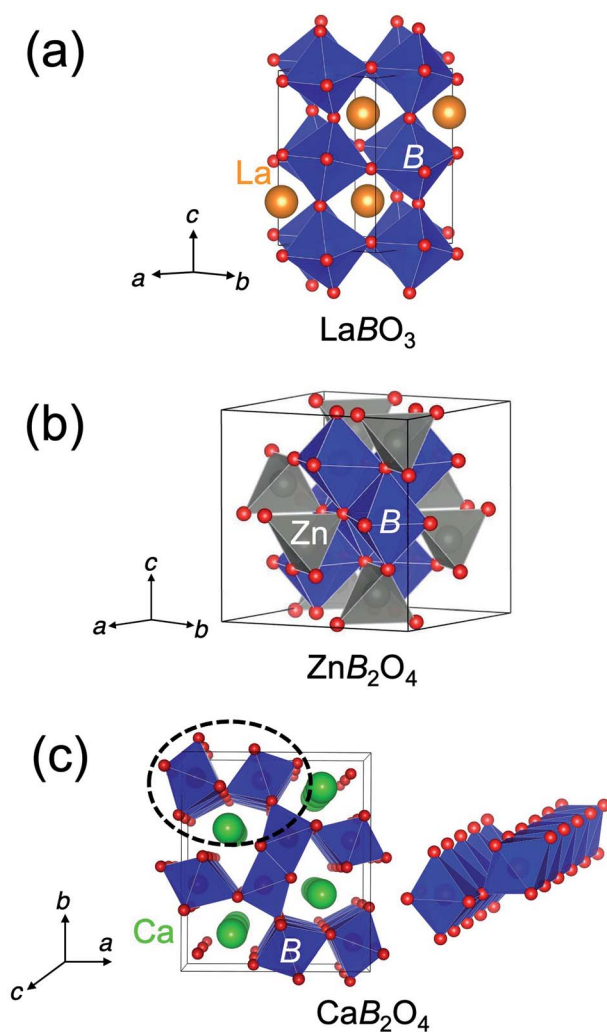


Fig. 1 Schematics of crystal structures of spinel (a) LaBO_3 , (b) ZnB_2O_4 , and (c) postspinel-structured CaB_2O_4 (CaFe_2O_4 -type). The one-dimensional edge-sharing BO_6 octahedral structure in the dashed circle is illustrated on the right.

participate in direct O–O bond formation based on density-functional-theory (DFT) calculations. Although the geometric feature associated with multi-site adsorption and reaction is reasonably described, the unusual 3-step reaction *via* simultaneous adsorption of two OH^- species on Fe CUSs (Fe_{CUS}) and two electrons transfer is assumed in this mechanism, in contrast to the ordinary 4-step reaction in which one OH^- and one electron are sequentially involved at each step.

The crystal structure of CaFe_2O_4 consists of edge-sharing FeO_6 octahedra chains like rutile. It can be classified as the postspinel structure, a high-pressure polymorph of spinel. Fig. 1 shows the crystal structures of perovskites, spinels, and postspinel. CaFe_2O_4 -type postspinel structure has the one-dimensional framework of octahedra with shared edges, including Ca ions in the voids, distinct from spinel and perovskite with the three-dimensional octahedral framework with shared edges and corners, respectively. Considering that the

OER activity of CaFe_2O_4 may be derived from the structural feature, the postspinel-related series of CaB_2O_4 ($B = \text{Cr}$ and Mn) must exhibit higher OER catalytic activity than the spinel or perovskite oxides.

In this paper, we investigated the OER catalytic activities of postspinel-structured CaB_2O_4 ($B = \text{Cr}$, Mn , and Fe) and systematically compared activities with perovskite LaBO_3 and spinel ZnB_2O_4 . Regardless of B -site transition metals, the OER activities in CaB_2O_4 oxides are monotonically superior to those of ZnB_2O_4 and LaBO_3 counterparts, which is supported by lower charge-transfer resistance in CaB_2O_4 . We performed DFT calculations to reveal the origin of OER activity in CaFe_2O_4 by remodeling the regular 4-step reaction mechanism from the previously reported 3-step mechanism¹⁷ and compared with the comparison with several possible mechanisms. We eventually found a novel 4-step reaction mechanism with lower theoretical overpotential, where the adsorbed oxygen on the Fe_{CUS} and the adjacent O_{BRI} were desorbed to generate oxygen. This finding suggests a new design principle for improving catalytic activity in multiple crystal structures of transition metal oxides.

Experimental

Material synthesis

CaCr_2O_4 , CaMn_2O_4 , and CaFe_2O_4 were obtained from the mixtures of CaCO_3 (99.95%) and Cr_2O_3 (99.9%), MnO_2 (99.99%), or Fe_2O_3 (99.99%) by calcining at 1473, 1473, and 1373 K, respectively, for 10–24 h for several times. ZnCr_2O_4 and ZnMn_2O_4 were synthesized from the mixtures of ZnO (99.9%) and Cr_2O_3 (99.9%) or MnO_2 (99.9%) by heating at 1273 and 1173 K for 5 and 10 h, respectively. ZnFe_2O_4 was obtained using the polymerized complex method.¹⁹ A mixture of ZnO (99.9%) and $\text{Fe}(\text{NO}_3)_3 \cdot 9\text{H}_2\text{O}$ (99.9%) at a molar ratio of 1 : 2 was dissolved in nitric acid solution (~ 5 M), to which a five-fold excess of citric acid and one-fold excess of 1,2-ethanediol were added to the solution with stirring. The resulting solution was heated for 573 K and maintained at this temperature for 1 h to dry. Subsequently, the dried powder was fired using a furnace at 673 K for 1 h and then 1273 K for 10 h in air with occasional grindings. LaCrO_3 and LaMnO_3 were also obtained using the polymerized complex method from mixtures of $\text{La}(\text{NO}_3)_3 \cdot 6\text{H}_2\text{O}$ and $\text{Cr}(\text{NO}_3)_3 \cdot 9\text{H}_2\text{O}$ or $\text{La}(\text{NO}_3)_3 \cdot 6\text{H}_2\text{O}$ and $\text{Mn}(\text{NO}_3)_3 \cdot 6\text{H}_2\text{O}$, by combustion at 1273 and 1073 K for 5 and 10 h, respectively. LaFeO_3 was synthesized from a stoichiometric mixture of La_2O_3 and Fe_2O_3 by heating at 1673 K for 10 h.

Basic characterization

The as-synthesized samples were identified by X-ray powder diffraction (XRD) with $\text{Cu-K}\alpha$ radiation (Ultima IV, Rigaku, Japan). The synchrotron XRD (SXRD) patterns were collected using a Debye–Scherrer camera installed at the BL02B2 beamline in SPring-8, Japan. The wavelength was determined as 0.49968 Å using CeO_2 as a reference. The SXRD data were analyzed using the Rietveld refinement program RIETAN-FP.²⁰ Specific surface areas were determined by Brunauer–Emmett–Teller (BET) analysis of Kr gas adsorption data (BELSORP-max,



MicrotracBEL, Japan). The morphologies of all the catalysts were confirmed by scanning electron microscopy (SEM) images (TM3030, Hitachi High-Tech, Japan). X-ray absorption near edge structure (XANES) spectra of Cr, Mn, and Fe K-edges were collected in the transmission mode at the BL14B2 beamline in SPring-8. The X-ray absorption spectra were normalized by spline functions between pre-edge and post-edge regions using Athena program of the IFEFFIT package.²¹

Electrochemical characterization

Working electrodes were prepared using the drop-casting method of inks containing catalysts on glassy carbon electrode, referred to previous papers.¹⁰ A 5 wt% proton-type Nafion suspension (Sigma-Aldrich), 0.1 M KOH aqueous solution (Nacalai Tesque, Inc., Japan), and tetrahydrofuran (THF, Sigma-Aldrich) were mixed at a ratio of 2 : 1 : 97 in volume. The catalyst ink was prepared by mixing 5 mg of catalyst, 1 mg of acetylene black (Denka Co., Ltd, Japan), and 1 mg of the THF solution. A 6.4 μL of catalyst ink was taken with stirring and drop cast onto the glassy-carbon disk electrode with 4 mm diameter.

Electrochemical measurements were conducted using a rotating-disk electrode rotator (RRDE-3 A, BAS Inc., Japan) and a bipotentiostat (model-2325, BAS Inc., Japan). We used a Pt wire electrode and a Hg/HgO electrode (International Chemistry Co., Ltd, Japan) filled with a 0.1 M KOH aqueous solution (Nacalai Tesque, Inc., Japan) as the counter and reference electrodes, respectively. All electrochemical measurements were conducted under O₂ saturation at room temperature. This fixed the equilibrium potential of the O₂/H₂O redox couple to 0.304 V *versus* (*vs.*) Hg/HgO. The disk potential was controlled between 0.3 and 0.9 V *vs.* Hg/HgO at a scan rate of 10 mV s⁻¹. The disk potential was represented in those *vs.* reversible hydrogen electrode (RHE), with *IR*-compensation ($R = 43 \Omega$). The capacitive effect was compensated by averaging the cathodic and anodic scans.

Chronoamperometry (CA) was conducted at 1.6 V *vs.* RHE, where *IR*-compensation was not made. The electrochemical surface area (ECSA) was determined by scanning non-faradaic region between 0.0 and 0.1 V *vs.* Hg/HgO, according to the literature.²² Electrochemical impedance spectroscopy (EIS) measurement was conducted using an electrochemical analyzer (760E, BAS Inc., Japan) at 1.7 V *vs.* RHE at frequencies ranging from 0.1 Hz to 1 MHz.

Density-functional-theory calculation

Bulk model electronic structure

Spin-polarized DFT calculations were systematically performed for spinel and postspinel oxides, namely, CaFe₂O₄, CaCr₂O₄, CaMn₂O₄, ZnCr₂O₄, ZnMn₂O₄, and ZnFe₂O₄, using the plane-wave based projector augmented wave (PAW) method as implemented in the Vienna *ab initio* Simulation Package (VASP).^{23–25} The generalized gradient approximation (GGA) parametrized by Perdew, Burke, and Ernzerhof (PBE)²⁶ were adopted to express exchange–correlation interactions. The

strong on-site coulombic interactions on the localized 3d electrons were treated with the GGA + *U* approach.²⁷ The $U_{\text{eff}} = 3.5, 4.0,$ and 3.9 eV were adopted for Cr, Mn, and Fe 3d orbitals, which were selected to reproduce the experimental oxidation enthalpy, as reported previously.^{28,29} The PAW potential data-set with radial cutoffs of 2.3 Å for Ca, Cr, Mn, Fe, Zn, and 1.52 Å for O were employed, where Ca-3s, 3p, 4s, Cr-3p, 3d, 4s, Mn-3p, 3d, 4s, Fe-3d, 4s, Zn-4s, 4p, 3d, O-2s, 2p were described as valence electrons. Table S11† summarizes the magnetic structures and nominal electron configurations considered in this work. The plane-wave cutoff energy was set to 500 eV for all calculations. The Brillouin zone was sampled using $k_1 \times k_2 \times k_3$ mesh points according to the Monkhorst–Pack scheme.³⁰ The mesh count for each direction was selected as the near natural number of 35 per lattice parameter (1 \AA^{-1}). The lattice constants and internal coordinates were optimized until the total energy difference and residual forces converged to less than 10^{-5} eV and 10^{-2} eV \AA^{-1} , respectively. According to literature,^{31–33} oxygen 2p band centers and unoccupied 3d band centers of transition metal atoms were computed from the projected density of states (DOS) as follows:

$$\varepsilon_{2p} = \frac{\int_{-\infty}^{E_F} E f_{2p}(E) dE}{\int_{-\infty}^{E_F} f_{2p}(E) dE}, \quad (1)$$

and

$$\varepsilon_{3d\text{-un}} = \frac{\int_{E_F}^{E_{\text{max}}} E f_{3d}(E) dE}{\int_{E_F}^{E_{\text{max}}} f_{3d}(E) dE}, \quad (2)$$

respectively. Here, $f_{2p}(E)$ and $f_{3d}(E)$ are DOS projected on O-2p and transition metal 3d orbitals, respectively; E_F is the Fermi energy; and E_{max} is the upper bound of unoccupied 3d bands. The E_{max} value was set as 10 eV higher than that of E_F . The number of conduction bands was increased until the shapes of projected DOS were converged.

Slab model surface energy and theoretical overpotential

The electronic structures of OER intermediates on the (001) surface of CaFe₂O₄ terminated by exposed FeO₅ pyramids were investigated using DFT calculations. The slab models in Fig. S6† were composed of doubled cells along the *c* and *b* axes for CaFe₂O₄. The number of layers and the length of the vacuum layer in the slab models were carefully determined by checking the convergences of surface energies. For the (001) plane in CaFe₂O₄, the slab models respectively consisted of 116 atoms with 8 layers. The lattice constants of slab models for CaFe₂O₄ were $9.29 \text{ \AA} \times 6.07 \text{ \AA} \times 43.1 \text{ \AA}$, including 20 Å vacuum layer to prevent interactions between surfaces in slab models. For these calculations, Brillouin zones were sampled with $4 \times 6 \times 1$ grids for CaFe₂O₄. We fixed the positions of 81 atoms in the middle of these models for CaFe₂O₄ to evaluate bare surface energies (blue areas in Fig. S6b†). The atomic positions were optimized except for atomic layers in the bottom of slab models (magenta areas in Fig. S6b†) to calculate surface energies. The other computational conditions, including the PAW data-set, U_{eff} values, plane-wave cutoff energies, total energy differences, and residual forces, were identical with bulk calculations.



The surface energies of CaFe_2O_4 under the equilibrium conditions in OER were calculated according to the procedure proposed in the literature.^{15,18} The surface Gibbs free energy can be described for CaFe_2O_4 as follows:

$$\Gamma = \frac{1}{2A} [E_{\text{DFT}}(\text{slab}) - N_{\text{O}}\mu_{\text{O}} - N_{\text{Ca}}\mu_{\text{Ca}} - N_{\text{Fe}}\mu_{\text{Fe}}], \quad (3)$$

where $E_{\text{DFT}}(\text{slab})$ is the total energy of the slab model using DFT calculations; A is the surface area of the slab model. N_{Z} and μ_{Z} ($\text{Z} = \text{Ca}, \text{Fe}, \text{and O}$) are defined as the number of the atoms in the slab model and chemical potentials, respectively. The chemical potentials are determined under the equilibrium condition of water splitting. In agreement with the computational hydrogen electrode model described in the literature,^{34,35} the chemical potential of oxygen can be expressed as a function of pH and ϕ , the potential difference between the working electrode and the reference electrode, as follows:

$$\mu_{\text{O}}(\text{pH}, \phi) = [E_{\text{DFT}}(\text{H}_2\text{O}(\text{g})) + [\text{ZPE-TS}]_{\text{H}_2\text{O}}] - [[E_{\text{DFT}}(\text{H}_2(\text{g})) + [\text{ZPE-TS}]_{\text{H}_2}] + 2(k_{\text{B}}T \ln a_{\text{H}^+} - e\phi)], \quad (4)$$

where $E_{\text{DFT}}(\text{H}_2\text{O}(\text{g}))$ and $E_{\text{DFT}}(\text{H}_2(\text{g}))$ are the total energies of H_2O and H_2 molecular, respectively; $[\text{ZPE-TS}]_{\text{H}_2\text{O}}$ and $[\text{ZPE-TS}]_{\text{H}_2}$ are the zero-point energy (ZPE) correction and entropy contribution, respectively; T is temperature; k_{B} is the Boltzmann constant; and a_{H^+} is the proton activity. The surface is regarded to be in equilibrium with the bulk CaFe_2O_4 phase. Then, the sum of the chemical potentials satisfies the following formula:

$$\mu_{\text{Ca}} + 2\mu_{\text{Fe}} + 4\mu_{\text{O}}(\text{pH}, \phi) = E_{\text{DFT}}(\text{CaFe}_2\text{O}_4) \quad (5)$$

where $E_{\text{DFT}}(\text{CaFe}_2\text{O}_4)$ is the total energy of bulk CaFe_2O_4 . By solving eqn (3) for μ_{Fe} and substituting it with eqn (4) into (3), the surface energy Γ is obtained as a linear function dependent on μ_{Ca} .

In this work, we constructed reaction mechanisms from reported AEM^{12,13} and lattice-oxygen-mediated mechanism (LOM)¹³ and conducted surface calculations for the mechanisms listed in Tables S12 and S13;† AEM- O_{BRI} , the LOM- O_{BRI} , AEM model, and dual-site AEM models referred by Sugawara *et al.*¹⁷ In these reaction steps, the *X/*Y surface state of postspinel-structured CaFe_2O_4 is determined as using the binding state *X for Fe_{CUS} and the binding state *Y for adjacent Fe_{CUS} with O_{BRI} . The - bondings of *O-O_{BRI} and $\text{*OOH-O}_{\text{BRI}}$ surfaces exhibit interactions between adsorbed oxygen and O_{BRI} . For each of the individual surfaces, the free energy change $\Delta G_{\text{*X/*Y}}$ (*X/*Y : adsorbed surfaces) was calculated using equations in Table S14.† For each of the six reaction mechanisms, the free energy change ΔG_n (n : reaction steps) in the individual reaction was defined as each formula in Tables S15 and S16.† Using the largest ΔG_n (n : reaction step), the value of theoretical overpotential (η_{th}) was calculated using the following equation:

$$\eta_{\text{th}} = \max\{\Delta G_1, \Delta G_2, \Delta G_3, \Delta G_4\}/e - 1.23 \text{ [V]}. \quad (6)$$

Results and discussion

Fig. 2 shows the XRD patterns of LaBO_3 , ZnB_2O_4 , and CaB_2O_4 ($B = \text{Cr}, \text{Mn}, \text{Fe}$). All samples crystallized in a single phase. CaB_2O_4 were assigned to orthorhombic phases, as reported previously.^{36–38} Rietveld refinement results obtained by using the SXRD data confirmed that the refined lattice parameters were similar to those previously reported in all samples (Fig. S1 and Tables S1–S9†). The calculated bond valence sums (BVSs) indicate trivalent states of transition metal ions, as expected from the simple ionic models of $\text{La}^{3+}\text{B}^{3+}\text{O}_3^{2-}$, $\text{Zn}^{2+}\text{B}_2^{3+}\text{O}_4^{2-}$, and $\text{Ca}^{2+}\text{B}_2^{3+}\text{O}_4^{2-}$. Fig. 3 shows the X-ray absorption spectra at K-edges of Cr, Mn, and Fe. The K-edge absorption positions of transition metals for perovskites, spinels, and postspinel are close to those of pure trivalent metal oxide references ($\text{B}_2^{3+}\text{O}_3$) rather than aliovalent references (B^{2+}O and B^{4+}O_2), although the differences in local structures around the B sites appeared in shapes in higher energy ranges than absorption energies. The structural and spectroscopic analyses exclude the possible effects of valence on OER activities,³³ thus the effects of crystal structure on activity can be investigated in this study.

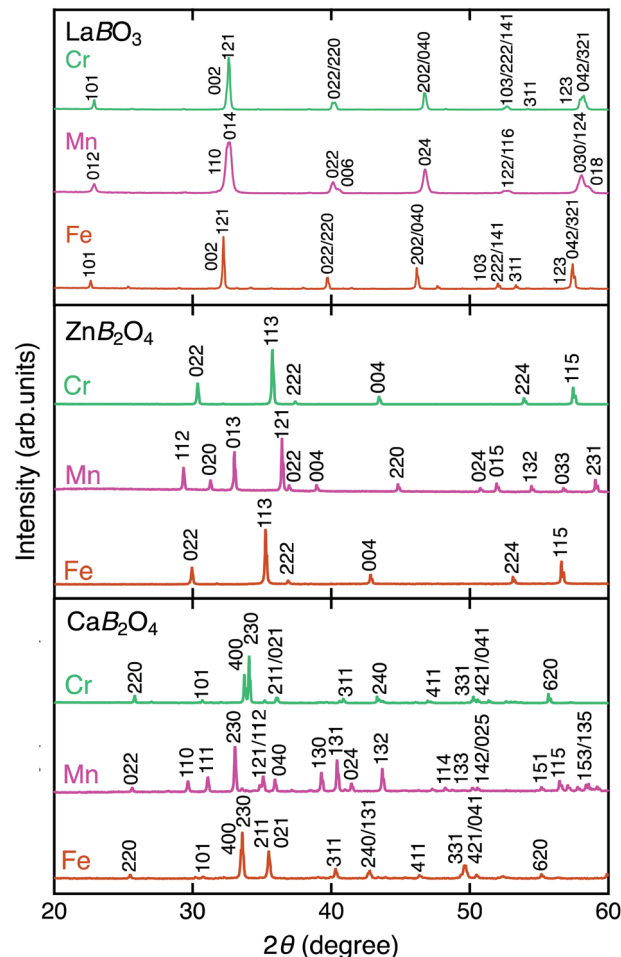


Fig. 2 XRD patterns of LaBO_3 , ZnB_2O_4 , and CaB_2O_4 for $B = \text{Cr}$ (green), Mn (magenta), and Fe (brown).



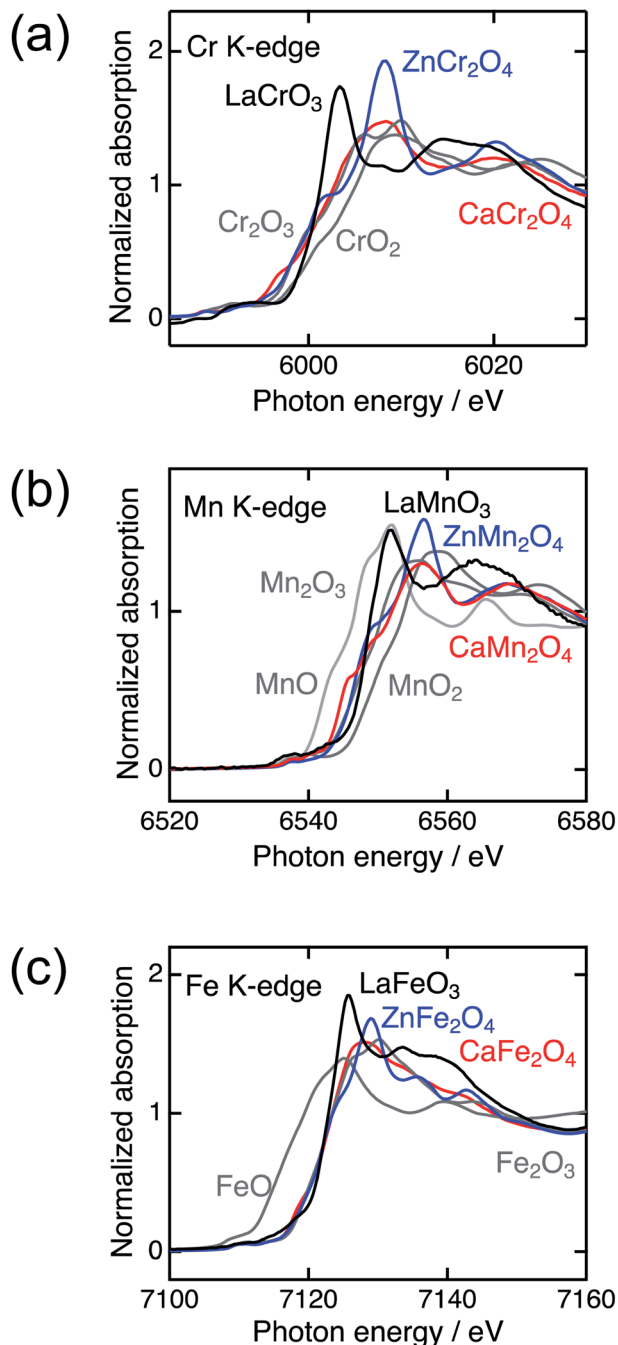


Fig. 3 X-ray absorption spectra of transition metal K-edges for LaBO_3 (black), ZnB_2O_4 (blue), CaB_2O_4 (red) ($B = \text{Cr, Mn, and Fe}$), and references (gray).

Specific surface areas determined by the BET analysis of Kr-gas adsorption data ranged in typical values between ~ 1.1 and $\sim 2.5 \text{ m}^2 \text{ g}^{-1}$, as listed in Table 1. The BET specific surface areas were adopted to normalize the current densities per surface area of catalysts in the electrochemical analysis. The values of ECSA in Table 1 were observed in the region of $10\text{--}27 \text{ m}^2 \text{ g}^{-1}$, displaying the same proportion of the maximum to the minimum, compared to that of BET surface areas. The SEM images in Fig. S2† indicate that the particle sizes roughly ranged

between 0.1 and $10 \mu\text{m}$ for all. The crucial differences in grain size were not observed between CaB_2O_4 and references containing the same B ion. The SEM observations roughly confirmed similar morphologies among all samples, compatible with BET and ECSA analyses.

Fig. 4 shows the linear sweep voltammograms for LaBO_3 , ZnB_2O_4 , and CaB_2O_4 ($B = \text{Cr, Mn, and Fe}$). Obviously, CaB_2O_4 series exhibited much higher activities than the LaBO_3 and ZnB_2O_4 counterparts in the identical transition metal element. Taking Cr oxides for instance, the overpotential of CaCr_2O_4 was $\eta_{0.05} = 0.34 \text{ V}$, substantially lower than those of ZnCr_2O_4 (0.44 V) and LaCrO_3 (0.75 V) (see the inset of Fig. 4a and Table 1), where the overpotentials ($\eta_{0.05}$) were determined at the onset potentials (E_{onset} V vs. RHE) exceeding the current density of $0.05 \text{ mA cm}_{\text{oxide}}^{-2}$: $\eta_{0.05} = E_{\text{onset}} - 1.23 \text{ (V)}$. The specific activity (a current density at 1.6 V vs. RHE) of CaCr_2O_4 was about 9 times higher than that of ZnCr_2O_4 or LaCrO_3 . Fig. 5 and Table 1 summarize the specific activities and overpotentials for all samples. The superiority of CaB_2O_4 as OER catalyst were commonly observed in the activities normalized by disk areas, ECSA, and BET surface areas (Fig. 5). Regardless of the constituent transition metals, the lower overpotentials and larger activities reveal the intrinsic superiority of the postspinel structures. Especially, CaFe_2O_4 exhibited about 30 times larger specific activity and 0.15 V smaller $\eta_{0.05}$ than ZnFe_2O_4 . The improvement from spinel-structured ZnFe_2O_4 to postspinel-structured CaFe_2O_4 was the most remarkable among all comparisons.

Significant differences between postspinel and other structures were observed in Tafel plots and EIS analyses. Fig. 6 shows the Tafel plots for LaBO_3 , ZnB_2O_4 , and CaB_2O_4 ($B = \text{Cr, Mn, and Fe}$). The Tafel slope of CaFe_2O_4 (53 mV dec^{-1}) was much smaller than that of ZnFe_2O_4 (102 mV dec^{-1}) and LaFeO_3 (78 mV dec^{-1}). Clear differences in Tafel slopes between postspinel-structured oxides and counterparts were also observed in Cr and Mn oxides. Since the Tafel slope varies in dependent on the rate-determining step (RDS),³⁹ the observed differences in Tafel slope indicate that the RDS is altered by crystal structures. Nyquist plots are displayed in Fig. 7 for LaBO_3 , ZnB_2O_4 , and CaB_2O_4 ($B = \text{Cr, Mn, and Fe}$). The semi-circles around $1\text{--}100 \text{ Hz}$ attributed to charge-transfer resistance (R_{ct}) changed depending on the crystal structure. The R_{ct} value of CaFe_2O_4 ($\sim 150 \Omega$) was smaller than that of LaFeO_3 ($\sim 400 \Omega$) and ZnFe_2O_4 ($\sim 7000 \Omega$). CaCr_2O_4 ($R_{\text{ct}} = \sim 2000 \Omega$) and CaMn_2O_4 ($\sim 800 \Omega$) exhibited lower R_{ct} values than LaBO_3 and ZnB_2O_4 counterparts. The fact that the R_{ct} values in CaCr_2O_4 and CaMn_2O_4 were larger than that in CaFe_2O_4 is probably associated with surface amorphizations in the formers, as shown in the HRTEM study later. The surface amorphizations disturb the charge transfer, deviating from the intrinsic nature of the crystalline surface. Consequently, the activated charge-transfer kinetics is consistently a primary origin for the enhanced OER activity in CaB_2O_4 for Cr, Mn, and Fe oxides.

We investigated the long-term stability and surface crystalline states of CaB_2O_4 . Fig. 8 shows the CA currents normalized by initial currents in CaCr_2O_4 , CaMn_2O_4 , and CaFe_2O_4 . CaFe_2O_4 exhibited no substantial degradation in OER activity. This



Table 1 Specific surface area from BET analysis and electrochemical surface area (ECSA) for LaBO_3 , ZnB_2O_4 , and CaB_2O_4 ($B = \text{Cr, Mn, Fe}$). Overpotential ($\eta_{0.05}$), specific activity normalized by BET surface area at 1.6 V vs. RHE, and Tafel slope for these catalysts

Compound	Specific surface area ($\text{m}^2 \text{g}^{-1}$)	ECSA ($\text{m}^2 \text{g}^{-1}$)	$\eta_{0.05}$ (V)	Specific activity ($\text{mA cm}_{\text{oxide}}^{-2}$)	Tafel slope (mV dec^{-1})
LaCrO_3	2.49	27.3	0.75	0.004	230
LaMnO_3	1.52	26.6	0.51	0.010	163
LaFeO_3	1.32	20.5	0.42	0.015	78
ZnCr_2O_4	1.84	15.3	0.47	0.008	248
ZnMn_2O_4	1.57	21.3	0.48	0.005	101
ZnFe_2O_4	1.15	10.9	0.45	0.009	103
CaCr_2O_4	1.15	18.2	0.31	0.068	138
CaMn_2O_4	1.32	17.5	0.39	0.012	84
CaFe_2O_4	1.11	10.3	0.33	0.111	53

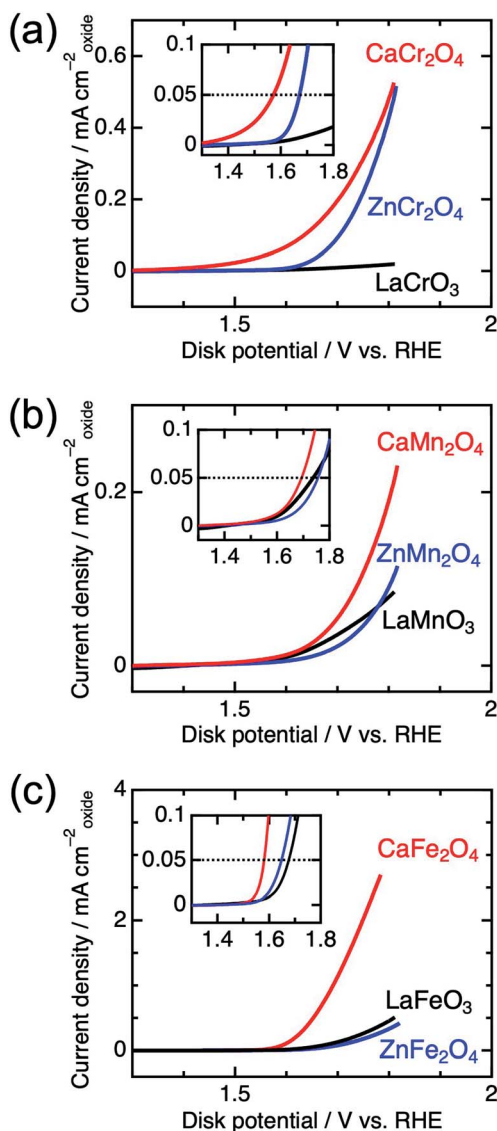


Fig. 4 Linear sweep voltammograms for LaBO_3 , ZnB_2O_4 , and CaB_2O_4 for $B =$ (a) Cr, (b) Mn, and (c) Fe. The insets represent the magnified data in the vicinity of the OER onset potential.

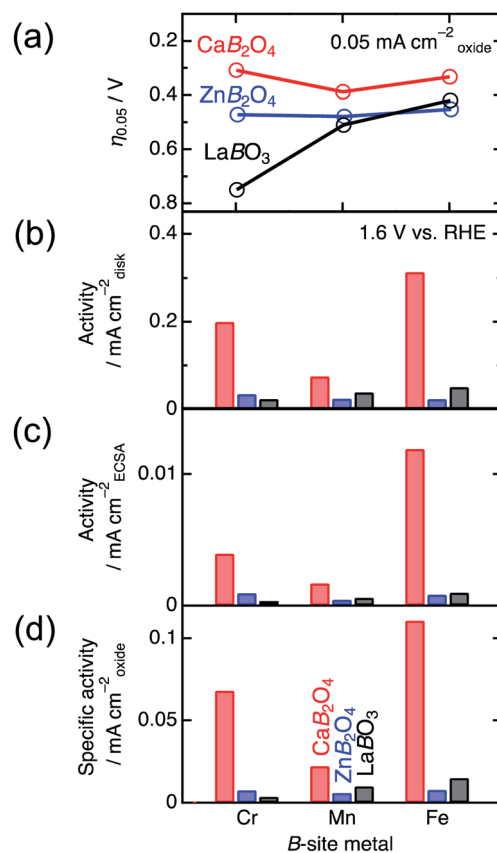


Fig. 5 Comparison of OER (a) overpotential ($\eta_{0.05}$) and activities at 1.6 V vs. RHE for LaBO_3 , ZnB_2O_4 , and CaB_2O_4 ($B = \text{Cr, Mn, and Fe}$) normalized by (b) disk area (0.126 cm^2), (c) ECSA, and (d) BET surface area.

observation manifests the robustness of CaFe_2O_4 in OER conditions, whereas the sudden drops in initial states for CaCr_2O_4 and CaMn_2O_4 (Fig. 8) indicate instability of surface crystalline states. Fig. S3[†] displays HRTEM images of CaCr_2O_4 , CaMn_2O_4 , and CaFe_2O_4 . CaFe_2O_4 retained the crystalline surface after CA, as well as the pristine and as-cast powders. In contrast, CaCr_2O_4 demonstrated severe surface amorphization



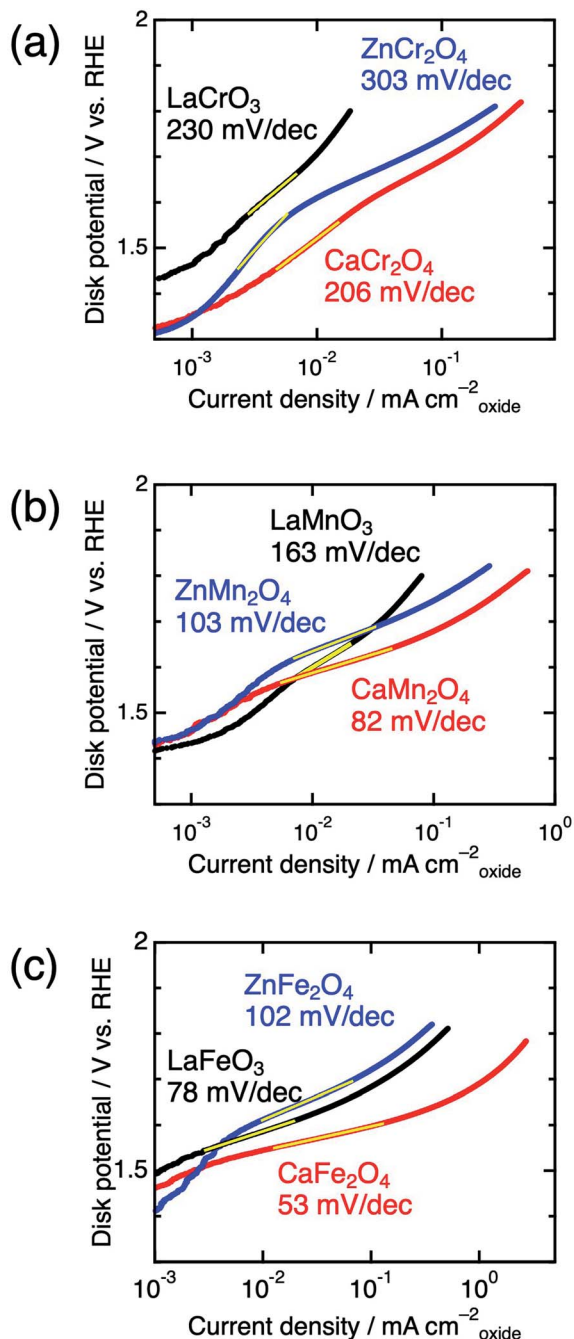


Fig. 6 Tafel plots of LaBO₃ (black), ZnB₂O₄ (blue), and CaB₂O₄ (red) for B = (a) Cr, (b) Mn, and (c) Fe.

even in the as-cast sample and further evolution of the amorphous layer after CA (Fig. 8). CaMn₂O₄ also possessed the amorphous surface in the as-cast sample, which is probably the cause of the initial degradation in CA. Gradual increases in current density were observed for several oxides (CaMn₂O₄ and CaFe₂O₄), but the origin was unclear at the present stage. Since CaFe₂O₄ did not exhibit severe amorphization, the intrinsic feature of the crystalline surface is predominantly reflected in the electrochemical analyses.

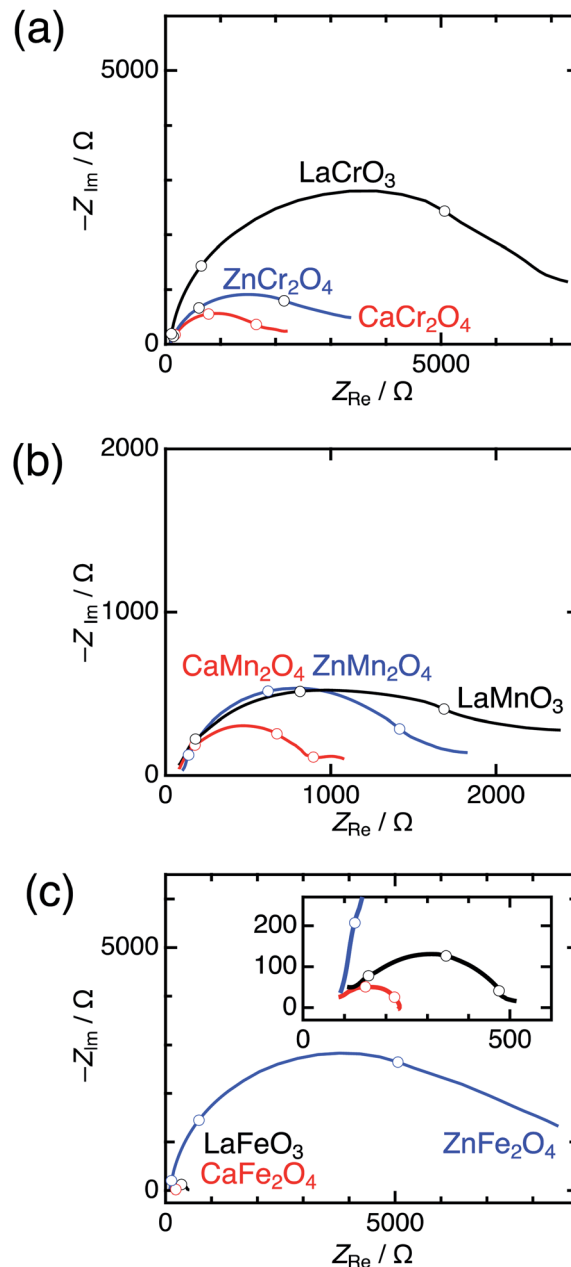


Fig. 7 Nyquist plots of LaBO₃ (black), ZnB₂O₄ (blue), and CaB₂O₄ (red) for B = (a) Cr, (b) Mn, and (c) Fe, measured at 1.7 V vs. RHE. The insets represent the magnified data in Fe oxides. Blank circles display points observed between 1–100 Hz.

Our electrochemical experiments elucidated that the OER catalytic activities in postspinel CaB₂O₄ (B = Cr, Mn, and Fe) are superior to those of perovskites LaBO₃ and spinels ZnB₂O₄, irrespective of B metal ions. The commonly observed properties in CaB₂O₄ suggest that the edge-sharing one-dimensional octahedra in postspinel structures predominate the reaction mechanism. We conducted DFT calculations to discuss the reaction mechanism on the surface of CaB₂O₄ associated with the geometric feature of the coordination polyhedra, in addition to the bulk electronic factors possibly affecting the OER catalysis. Fig. S4† shows the DOS generated from bulk-model DFT



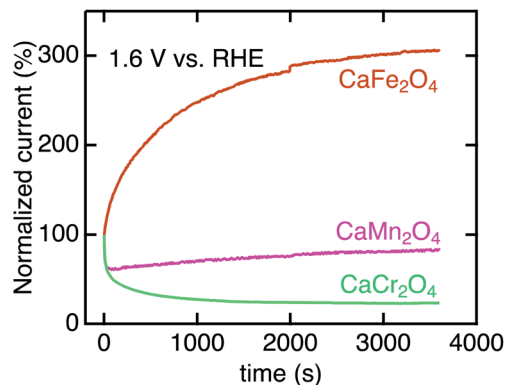


Fig. 8 Chronoamperometry of CaB_2O_4 for $B = \text{Cr, Mn, and Fe}$ normalized initial current values. The data were collected at 1.6 V vs. RHE after three CV scans.

calculations for spinels and postspinel. All ZnB_2O_4 and CaB_2O_4 ($B = \text{Cr, Mn, Fe}$) displayed insulating band structures with band gaps of $\sim 1\text{--}2$ eV, finding no definite difference between spinel and postspinel structures. Typical OER descriptors of O-2p band center⁴⁰ and charge-transfer energy (Δ)⁴¹ were close between ZnB_2O_4 and CaB_2O_4 (Table S10[†]). Unlike the linear tendency in the $\eta_{0.05}$ vs. Δ plots for the perovskite oxides,³² there was no clear trend (Fig. S5[†]) in the spinels and postspinel in this study. Hence, almost isoelectronic states in the bulk form cannot explain the origin of OER activity in the postspinel-structured oxides.

To evaluate credible information on the OER on postspinel, we calculated the theoretical overpotentials from the surface free-energies. In the surface-state calculations, CaFe_2O_4 was selected because of its robust crystalline surface in OER conditions, as demonstrated in CA and HRTEM studies. The calculations of surface states were conducted on the (001) plane with O_{BRI} ions bridged by two Fe ions, referring to the reaction mechanism in RuO_2 with one-dimensionally aligned octahedra.^{4,5} We originally investigated three different reaction mechanisms AEM- O_{BRI} , LOM- O_{BRI} , and AEM. Fig. 9 shows the surface geometries after structural relaxations. First, in the AEM- O_{BRI} (Fig. 9a), the calculations were performed using conventional adsorbates, $^*\text{OH}$, $^*\text{O}$, and $^*\text{OOH}$ binding to Fe_{CUS} on the surface containing O_{BRI} . The structural relaxation revealed the formation of additional bonds between adsorbed oxygen (O_{ad}) and O_{BRI} when $^*\text{O}$ and $^*\text{OOH}$ species are adsorbed ($^*\text{O}-\text{O}_{\text{BRI}}$ and $^*\text{OOH}-\text{O}_{\text{BRI}}$ states). These bond formations indicate that O_{BRI} participates in the OER on the CaFe_2O_4 surface. Second, we examined the lattice oxygen mechanism⁴² (LOM- O_{BRI} , Fig. 9b) in which OH^- is adsorbed to Fe_{CUS} (step 1: $^*/- + \text{OH}^- \rightarrow ^*\text{OH}/- + \text{e}^-$), and desorbed with O_{BRI} to evolve O_2 (step 2: $^*\text{OH}/- + \text{OH}^- \rightarrow ^*/ + \text{O}_2 + \text{H}_2\text{O} + \text{e}^-$). Third, we considered the AEM mechanism, where the adsorbates are solely bound to Fe_{CUS} because of the absence of the O_{BRI} atom (Fig. 9c). This mechanism is similar to the conventional OER mechanism in single-site adsorption.

The free energies $\Delta G_{^*X/^*Y}$ at each reaction step of the above-examined models are listed in Table S17[†] defined with formulae in Table S14.[†] The value of $\Delta G_{^*X/^*Y}$ tended to increase in correspondence with the number of adsorbed atoms in the $^*X/^*Y$ surface state. We calculated the values of energy change ΔG_n of each reaction steps and η_{th} for the six reaction mechanisms (Table S18[†]) as following calculations in formulae in Tables S15 and S16.[†] Fig. 10 shows the energy diagrams for each reaction mechanism. In Fig. 10, the thick lines represent the potential determining steps (PDSs) with the largest ΔG_n in each mechanism, accompanied by η_{th} values calculated from ΔG_n at PDSs. The PDSs for AEM- O_{BRI} ($\eta_{\text{th}} = 1.33$ V) and LOM- O_{BRI} ($\eta_{\text{th}} = 0.85$ V) were assigned to step 3 ($^*\text{O}-\text{O}_{\text{BRI}} + \text{OH}^- \rightarrow ^*\text{OOH}-\text{O}_{\text{BRI}} + \text{e}^-$) and step 4 ($^*/^*\text{OH} + \text{OH}^- \rightarrow ^*/- + \text{H}_2\text{O} + \text{e}^-$), respectively. In contrast, step 2 with a significant large η_{th} (2.04 V) was the PDS in the AEM ($^*\text{OH}/^* + \text{OH}^- \rightarrow ^*\text{O}/^* + \text{H}_2\text{O} + \text{e}^-$). LOM- O_{BRI} demonstrated the lowest η_{th} among the 4-step mechanisms. Due to the high variation in surface structures and types of adsorbed species in PDSs, we could not identify any consistency in adsorption states of PDSs among the three reaction mechanisms. The PDSs of LOM- O_{BRI} and AEM were categorized as transforming steps from $^*\text{OH}$ to $^*\text{O}$, whereas the PDSs of AEM- O_{BRI} were assigned to adsorption processes of the reactant OH^- . We conclude that the LOM- O_{BRI} with the lowest η_{th} (0.85 V) examined in the present DFT calculation is the most probable mechanism to explain the high OER activity of postspinel-structured oxides.

We compared theoretical overpotential in the mechanisms reported in previous studies with LOM- O_{BRI} , which is the most probable reaction mechanism among our reaction mechanisms described above. We validated two types of 4-step mechanisms, dual-site AEM (1)–(2) in Fig. 9d and e, which are reformulations of the 3-step model, and dual-site AEM (3) (Fig. 9f), proposed by Sugawara *et al.*¹⁷ The OH^- adsorbates are sequentially bonded with two Fe_{CUS} sites in the 4-step reaction with two procedures [$^*/^* \rightarrow ^*\text{OH}/^* \rightarrow ^*\text{OH}/^*\text{OH} \rightarrow ^*\text{OH}/-$ (Fig. 9d) or $^*/^* \rightarrow ^*/^*\text{OH} \rightarrow ^*\text{OH}/^*\text{OH} \rightarrow ^*\text{OH}/-$ (Fig. 9e)], in contrast to the simultaneous OH^- adsorption in the previous 3-step reaction in Fig. 9f ($^*/^* \rightarrow ^*\text{OH}/^*\text{OH} \rightarrow ^*\text{OH}/^*\text{O}$). In dual-site AEMs, depending on the initial position of $^*\text{OH}$ species, the PDSs were determined at adsorption of step 2 in dual-site AEM (1) ($\eta_{\text{th}} = 1.11$ V, $^*/^*\text{OH} + \text{OH}^- \rightarrow ^*\text{OH}/^*\text{OH} + \text{e}^-$), and step 1 in dual-site AEM (2) ($\eta_{\text{th}} = 0.88$ V, $^*/^* + \text{OH}^- \rightarrow ^*\text{OH}/^* + \text{e}^-$). The calculation using the 3-step mechanism “dual-site AEM (3)” referred to the previous study¹⁷ demonstrated simultaneous adsorptions of reactants (step 1) was assigned to the PDS ($\eta_{\text{th}} = 1.00$ V, $^*/^* + 2\text{OH}^- \rightarrow ^*\text{OH}/^*\text{OH} + 2\text{e}^-$). The present calculations revealed that the PDSs in three subpaths of dual-site AEMs are assigned in adsorptions steps of OH^- species to the surface, differing from the charge-transfer PDS in the previous study,¹⁷ whereas the original PDS reaction ($^*\text{OH}/^*\text{OH} + \text{OH}^- \rightarrow ^*\text{OH}/- + \text{H}_2\text{O} + \text{e}^-$) was stabilized in our calculations. Since the repulsive energies between the two OH^- species were not considered, the theoretical overpotential (0.58 V)¹⁷ in the previous 3-step reaction mechanism would be underestimated.



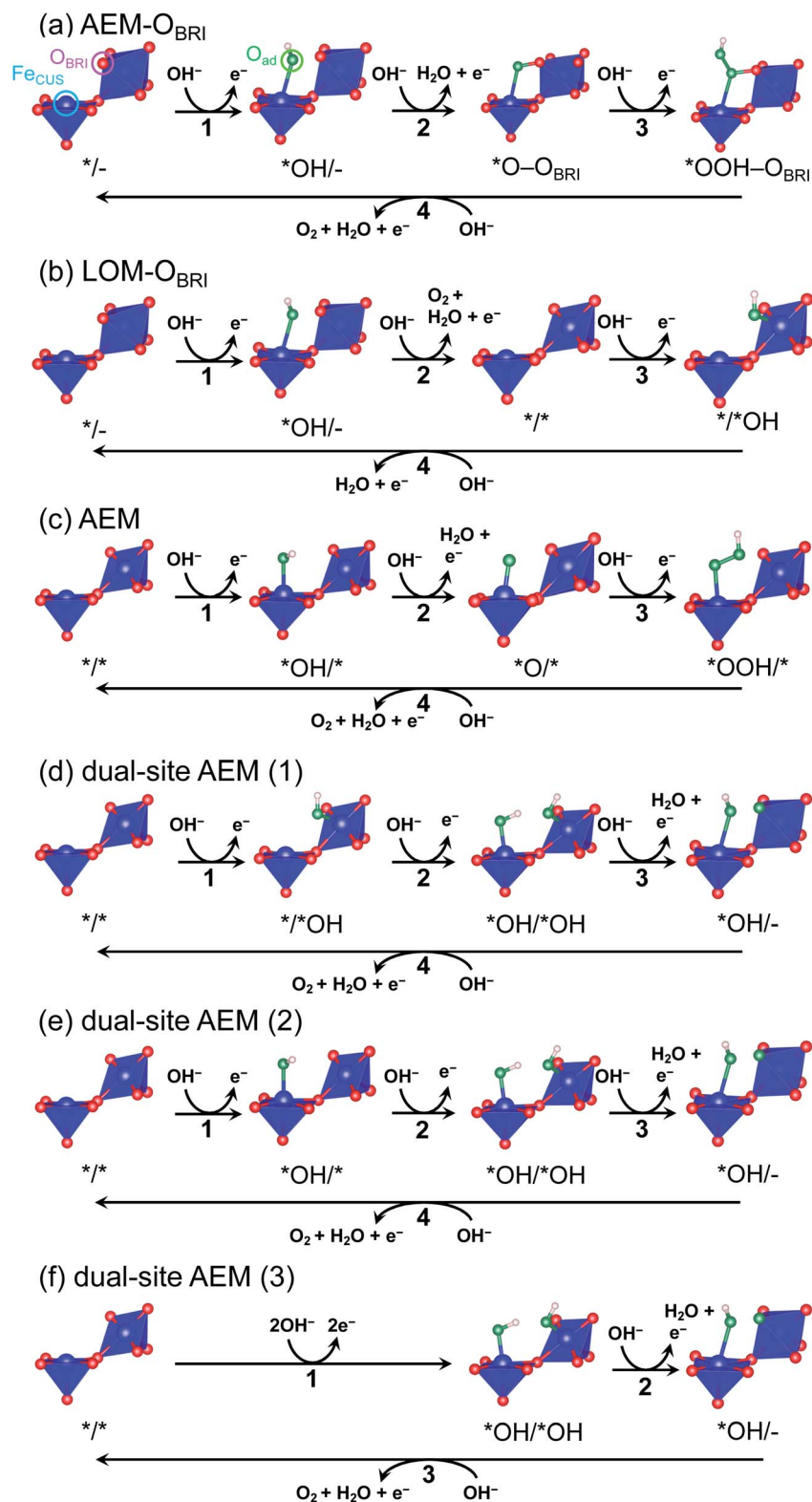


Fig. 9 Schematics of surface structures of CaFe_2O_4 after structural relaxations for mechanisms of (a) AEM-O_{BRI}, (b) LOM-O_{BRI}, (c) AEM, and dual-site AEMs. In dual-site AEM, calculated mechanisms start from the surface of (d) $\text{*/} + \text{OH}$, (e) *OH/* , and (f) *OH/* .



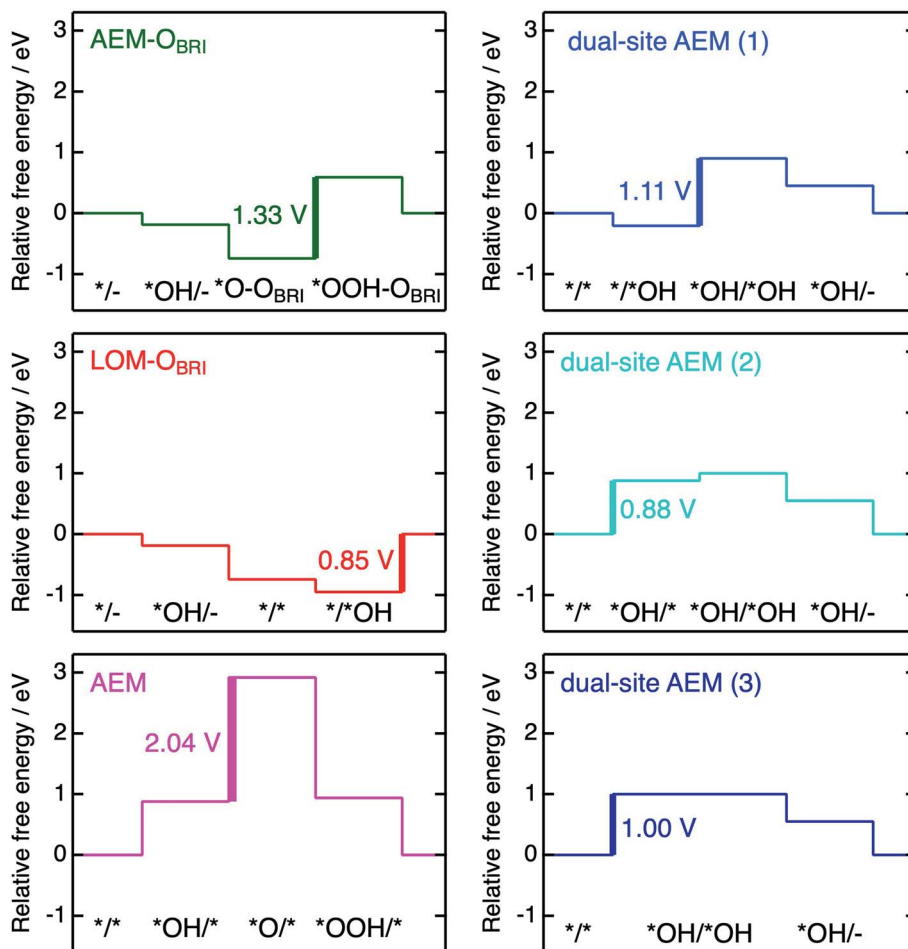


Fig. 10 Energy diagrams for the mechanisms of AEM–O_{BRI}, LOM–O_{BRI}, AEM (left), and three types of dual-site AEMs (right). Thick lines and values correspond to PDSs and η_{th} , respectively. Each relative free energy was calculated in $\phi = 1.23$ V.

Conclusion

In summary, we investigated the OER catalytic activity in the postspinel-structured oxides CaB₂O₄ (B = Cr, Mn, and Fe), revealing higher OER activities and smaller charge-transfer resistances than the perovskite- and spinel-structured counterparts. The DFT calculation on the surface of CaFe₂O₄ elucidates that a novel reaction mechanism with the lowest theoretical overpotential, where O_{BRI} and O_{ad} are combined to generate oxygen, is more probable than the 3-step reaction mechanism with simultaneous adsorption of OH[−] proposed in the previous study. Consequently, the geometric configurations around adsorption sites tolerating additional bonding are another factor to activate OER beyond the conventional single-site OER mechanism.

Conflicts of interest

There are no conflicts to declare.

Acknowledgements

The authors thank Hiroyuki Inoue for discussions about EIS analysis and Enago (www.enago.jp) for the English language

review. The synchrotron radiation experiments were performed at SPring-8 with the approval of JASRI (proposal number 2018B1769, 2019A1476, and 2019A1650). This work was supported by JSPS KAKENHI (grant number JP16H04220, JP17K18973, JP17K19182, JP18H03835, JP20H02825, JP20H05180, and JP20H05192), Murata Science Foundation, and Takahashi Industrial and Economic Research Foundation.

References

- W. T. Hong, M. Risch, K. A. Stoerzinger, A. Grimaud, J. Suntivich and Y. Shao-Horn, *Energy Environ. Sci.*, 2015, **8**, 1404–1427.
- E. Fabbri, A. Habereder, K. Waltar, R. Kötz and T. J. Schmidt, *Catal. Sci. Technol.*, 2014, **4**, 3800–3821.
- Y. Jiao, Y. Zheng, M. Jaroniec and S. Z. Qiao, *Chem. Soc. Rev.*, 2015, **44**, 2060–2086.
- R. R. Rao, M. J. Kolb, L. Giordano, A. F. Pedersen, Y. Katayama, J. Hwang, A. Mehta, H. You, J. R. Lunger, H. Zhou, N. B. Halck, T. Vegge, I. Chorkendorff, I. E. L. Stephens and Y. Shao-Horn, *Nat. Catal.*, 2020, **3**, 516–525.



- 5 R. R. Rao, M. J. Kolb, N. B. Halck, A. F. Pedersen, A. Mehta, H. You, K. A. Stoerzinger, Z. Feng, H. A. Hansen, H. Zhou, L. Giordano, J. Rossmeisl, T. Vegge, I. Chorkendorff, I. E. L. Stephens and Y. Shao-Horn, *Energy Environ. Sci.*, 2017, **10**, 2626–2637.
- 6 S. Trasatti, *J. Electroanal. Chem. Interfacial Electrochem.*, 1980, **111**, 125–131.
- 7 J. R. Swierk, S. Klaus, L. Trotochaud, A. T. Bell and T. D. Tilley, *J. Phys. Chem. C*, 2015, **119**, 19022–19029.
- 8 H. Wang, K. H. L. Zhang, J. P. Hofmann, V. A. de la Peña O'Shea and F. E. Oropeza, *J. Mater. Chem. A*, 2021, **9**, 19465–19488.
- 9 Q. Zhao, Z. Yan, C. Chen and J. Chen, *Chem. Rev.*, 2017, **117**, 10121–10211.
- 10 J. Suntivich, H. A. Gasteiger, N. Yabuuchi, H. Nakanishi, J. B. Goodenough and Y. Shao-Horn, *Nat. Chem.*, 2011, **3**, 546–550.
- 11 S. F. Hung, Y. Y. Hsu, C. J. Chang, C. S. Hsu, N. T. Suen, T. S. Chan and H. M. Chen, *Adv. Energy Mater.*, 2018, **8**, 1701686.
- 12 J. O. M. Bockris and T. Otagawa, *J. Phys. Chem.*, 1983, **87**, 2960–2971.
- 13 J. Song, C. Wei, Z. F. Huang, C. Liu, L. Zeng, X. Wang and Z. J. Xu, *Chem. Soc. Rev.*, 2020, **49**, 2196–2214.
- 14 D. Guan, K. Zhang, Z. Hu, X. Wu, J. L. Chen, C. W. Pao, Y. Guo, W. Zhou and Z. Shao, *Adv. Mater.*, 2021, **33**, 1–12.
- 15 A. Takamatsu, I. Yamada, S. Yagi and H. Ikeno, *J. Phys. Chem. C*, 2017, **121**, 28403–28411.
- 16 I. Yamada, H. Fujii, A. Takamatsu, H. Ikeno, K. Wada, H. Tsukasaki, S. Kawaguchi, S. Mori and S. Yagi, *Adv. Mater.*, 2017, **29**, 1603004.
- 17 Y. Sugawara, K. Kamata, A. Ishikawa, Y. Tateyama and T. Yamaguchi, *ACS Appl. Energy Mater.*, 2021, **4**, 3057–3066.
- 18 C. F. Dickens and J. K. Nørskov, *J. Phys. Chem. C*, 2017, **121**, 18516–18524.
- 19 M. Kakihana, *J. Sol-Gel Sci. Technol.*, 1996, **6**, 7–55.
- 20 F. Izumi and K. Momma, *Solid State Phenom.*, 2007, **130**, 15–20.
- 21 B. Ravel and M. Newville, *J. Synchrotron Radiat.*, 2005, **12**, 537–541.
- 22 C. C. L. McCrory, S. Jung, I. M. Ferrer, S. M. Chatman, J. C. Peters and T. F. Jaramillo, *J. Am. Chem. Soc.*, 2015, **137**, 4347–4357.
- 23 P. E. Blochl, *Phys. Rev. B: Condens. Matter Mater. Phys.*, 1994, **50**, 17953–17979.
- 24 G. Kresse and J. Furthmüller, *Phys. Rev. B: Condens. Matter Mater. Phys.*, 1996, **54**, 11169–11186.
- 25 G. Kresse, *Comput. Mater. Sci.*, 1996, **6**, 15–50.
- 26 J. P. Perdew, K. Burke and M. Ernzerhof, *Phys. Rev. Lett.*, 1996, **77**, 3865–3868.
- 27 S. L. Dudarev, G. A. Botton, S. Y. Savrasov, C. J. Humphreys and A. P. Sutton, *Phys. Rev. B: Condens. Matter Mater. Phys.*, 1998, **57**, 1505–1509.
- 28 Y. Wang and G. Guo, *Phys. Rev. B: Condens. Matter Mater. Phys.*, 2006, **73**, 64424.
- 29 Z. Hu and H. Metiu, *J. Phys. Chem. C*, 2011, **115**, 5841–5845.
- 30 H. J. Monkhorst and J. D. Pack, *Phys. Rev. B: Condens. Matter Mater. Phys.*, 1976, **13**, 5188–5192.
- 31 A. Grimaud, K. J. May, C. E. Carlton, Y. L. Lee, M. Risch, W. T. Hong, J. Zhou and Y. Shao-Horn, *Nat. Commun.*, 2013, **4**, 2439.
- 32 I. Yamada, A. Takamatsu, K. Asai, H. Ohzuku, T. Shirakawa, T. Uchimura, S. Kawaguchi, H. Tsukasaki, S. Mori, K. Wada, H. Ikeno and S. Yagi, *ACS Appl. Energy Mater.*, 2018, **1**, 3711–3721.
- 33 I. Yamada, A. Takamatsu, K. Asai, T. Shirakawa, H. Ohzuku, A. Seno, T. Uchimura, H. Fujii, S. Kawaguchi, K. Wada, H. Ikeno and S. Yagi, *J. Phys. Chem. C*, 2018, **122**, 27885–27892.
- 34 J. Rossmeisl, A. Logadottir and J. K. Nørskov, *Chem. Phys.*, 2005, **319**, 178–184.
- 35 I. C. Man, H.-Y. Su, F. Calle-Vallejo, H. A. Hansen, J. I. Martínez, N. G. Inoglu, J. Kitchin, T. F. Jaramillo, J. K. Nørskov and J. Rossmeisl, *ChemCatChem*, 2011, **3**, 1085.
- 36 W. H. Hartford, K. A. Lane and W. A. Meyer, *J. Am. Chem. Soc.*, 1950, **72**, 3353–3356.
- 37 Y. Matsumoto, M. Obata and J. Hombo, *J. Phys. Chem.*, 1994, **98**, 2950–2951.
- 38 C. D. Ling, J. J. Neumeier and D. N. Argyriou, *J. Solid State Chem.*, 2001, **160**, 167–173.
- 39 T. Shinagawa, A. T. Garcia-Esparza and K. Takanabe, *Sci. Rep.*, 2015, **5**, 13801.
- 40 A. Grimaud, K. J. May, C. E. Carlton, Y. L. Lee, M. Risch, W. T. Hong, J. Zhou and Y. Shao-Horn, *Nat. Commun.*, 2013, **4**, 2439.
- 41 W. T. Hong, K. A. Stoerzinger, Y.-L. L. Lee, L. Giordano, A. Grimaud, A. M. Johnson, J. Hwang, E. J. Crumlin, W. Yang and Y. Shao-Horn, *Energy Environ. Sci.*, 2017, **10**, 2190–2200.
- 42 J. S. Yoo, X. Rong, Y. Liu and A. M. Kolpak, *ACS Catal.*, 2018, **8**, 4628–4636.

